

The relationship between local structure and photo-Fenton catalytic ability of glasses and glass-ceramics prepared from Japanese slag

ALI, Ahmed S <<http://orcid.org/0000-0001-9943-5220>>, NOMURA, Kiyoshi, HOMONNAY, Zoltan, KUZMANN, Erno, SCRIMSHIRE, Alex <<http://orcid.org/0000-0002-6828-3620>>, BINGHAM, Paul A <<http://orcid.org/0000-0001-6017-0798>>, KREHULA, Stjepko, RISTIĆ, Mira, MUSIĆ, Svetozar and KUBUKI, Shiro

Available from Sheffield Hallam University Research Archive (SHURA) at:

<https://shura.shu.ac.uk/25058/>

This document is the Accepted Version [AM]

Citation:

ALI, Ahmed S, NOMURA, Kiyoshi, HOMONNAY, Zoltan, KUZMANN, Erno, SCRIMSHIRE, Alex, BINGHAM, Paul A, KREHULA, Stjepko, RISTIĆ, Mira, MUSIĆ, Svetozar and KUBUKI, Shiro (2019). The relationship between local structure and photo-Fenton catalytic ability of glasses and glass-ceramics prepared from Japanese slag. *Journal of Radioanalytical and Nuclear Chemistry*. [Article]

Copyright and re-use policy

See <http://shura.shu.ac.uk/information.html>

Title page

Names of the authors: Ahmed S. Ali¹, Kiyoshi Nomura¹, Zoltan Homonnay²,
Erno Kuzmann², Alex Scrimshire³, Paul A. Bingham³, Stjepko Krehula⁴, Mira Ristić⁴,
Svetozar Musić⁴, Shiro Kubuki¹

Title: The relationship between local structure and photo-Fenton catalytic ability of glasses
and glass-ceramics prepared from Japanese slag

Affiliations and addresses of the authors:

1. Department of Chemistry, Graduate School of Science and Engineering, Tokyo
Metropolitan University, 1-1 Minami-Osawa, Hachi-Oji, Tokyo 192-0397, Japan
2. Institute of Chemistry, Eötvös Loránd University, Pázmány P. s. 1/A, Budapest, 1117,
Hungary
3. Faculty of Science, Technology and Arts, Sheffield Hallam University, Howard Street,
Sheffield S1 1WB, UK
4. Division of Materials Chemistry, Ruđer Bosković Institute, Bijenička c. 54, 10000
Zagreb, Croatia

E-mail address of the corresponding author: Balasfora2000@yahoo.com

The relationship between local structure and photo-Fenton catalytic ability of glasses and glass-ceramics prepared from Japanese slag

A. S. Ali¹, K. Nomura¹, Z. Homonnay², E. Kuzmann², A. Scrimshire³, P. A. Bingham³, S. Krehula⁴, M. Ristić⁴, S. Musić⁴, S. Kubuki¹

1. Department of Chemistry, Graduate School of Science and Engineering, Tokyo Metropolitan University, 1-1 Minami-Osawa, Hachi-Oji, Tokyo 192-0397, Japan

2. Institute of Chemistry, Eötvös Loránd University, Pázmány P. s. 1/A, Budapest, 1117, Hungary

3. Faculty of Science, Technology and Arts Sheffield Hallam University, Howard Street, Sheffield S1 1WB, UK

4. Division of Materials Chemistry, Ruđer Bosković Institute, Bijenička c. 54, 10000 Zagreb, Croatia

Abstract

Local structure and the photo-Fenton reactivity of iron-containing glasses and glass-ceramics prepared from Japanese domestic waste slag were investigated. The largest rate constant (k) of $(2.8 \pm 0.08) \times 10^{-2} \text{ min}^{-1}$ was recorded for the methylene blue degradation test by using H_2O_2 with a heat-treated ‘model slag’. The ^{57}Fe Mössbauer spectrum was composed of a paramagnetic doublet with isomer shift of $0.18 \pm 0.01 \text{ mm s}^{-1}$ attributed to

distorted $\text{Fe}^{\text{III}}\text{O}_4$ tetrahedra. These results indicate that the paramagnetic Fe^{3+} provided strong photo-Fenton catalytic ability, and that waste slag can thus be recycled as an effective visible-light activated photocatalyst.

Article Highlights

- 1- Waste slag was used to prepare glass samples for photocatalytic applications.
- 2- The degradation of methylene blue solution was enhanced by adding hydrogen peroxide.
- 3- Irradiating the samples with sunlight has a positive effect on the catalyst performance.

Keywords

Domestic waste slag; ^{57}Fe -Mössbauer spectroscopy; visible-light activated photocatalytic effect; photo-Fenton reaction; methylene blue; Iron oxide

1- Introduction

Waste materials are a severe problem worldwide. The Organization for Economic Co-operation and Development (OECD) reported that the annual total amount of municipal waste discarded from the OECD affiliated countries exceeds an estimated 650 million tons (522 kg per capita) [1]. Hence, recycling or reuse of waste material is becoming essential. In Japan and other countries, incineration plants have been established to meet the lack of landfill sites. The by-product of the incineration plants is slag, which is mainly used at present as civil engineering filler materials and as raw materials for the cement industry [2].

On the other hand, organic pollutants in wastewater are a significant problem worldwide. Since its discovery in Japan in 1972 by Fujishima and Honda [3], materials with photocatalytic activity have received great interest and a number of applications. The applications of photocatalytic materials that mineralize and decompose organic pollutants

have drawn a lot of benefits. Photoactivity using TiO_2 is a good solution for the degradation of organic materials, however, its photoactivity can only be activated under UV light due to the wide band gap of TiO_2 , 3.2 eV. Various conventional semiconductors have been tested as low bandgap photocatalysts. Among these, Fe_2O_3 is low cost, has a narrow band gap of 2.2 eV, is non-toxic, chemically stable and is thus an environmentally friendly material [4].

If the slag discarded from combustion plants, which contains Fe_2O_3 , can be used as a photocatalytic material, this will be a low-cost alternative to high-cost materials such as TiO_2 , and can thus enhance application of this technology whilst increasing the economic return from incineration plants. Some research refers to the possibility of achieving such a goal, for example Kubuki *et al.* [5] reported that $15\text{Na}_2\text{O}\cdot15\text{CaO}\cdot50\text{Fe}_2\text{O}_3\cdot20\text{SiO}_2$ (weight %) glass showed a visible-light activated photocatalytic effect. The sample after heat treatment at 1000 °C for 100 min caused decomposition of 10 $\mu\text{mol L}^{-1}$ methylene blue (MB) with a first-order rate constant (k) of $4.78 \times 10^{-4} \text{ min}^{-1}$ [5]. Iron-containing aluminosilicate glass, which has a similar composition to slag, $15\text{Na}_2\text{O}\cdot15\text{CaO}\cdot40\text{Fe}_2\text{O}_3\cdot11\text{Al}_2\text{O}_3\cdot19\text{SiO}_2$ (weight %), also showed a photocatalytic effect after heat treatment at 1000 °C for 100 min, having a larger k of $9.26 \times 10^{-3} \text{ min}^{-1}$ for MB degradation [6]. It is noted that the visible-light activated photocatalytic effect of iron-containing silicate glass was enhanced by introducing Al_2O_3 . Kubuki *et al.* [7, 8] also reported that iron silicate glass prepared by recycling the ash discharged from municipal solid waste combustion plant (MSW ash) was effective in reducing the chemical oxygen demand (COD) of artificial wastewater [7, 8].

Ishikawa *et al.* [9] reported that heat treatment of waste slag recycled glass-ceramics (WSRG) with additional Fe_2O_3 content of 10, 30 and 50 mass % decomposed MB aqueous solution with a first-order rate constant (k) of 2.6×10^{-3} , 2.3×10^{-3} and $2.7 \times 10^{-3} \text{ min}^{-1}$, respectively, under visible-light irradiation. The absorption area for the fitted $\alpha\text{-Fe}_2\text{O}_3$ component in ^{57}Fe -Mössbauer spectra showed an almost identical amount of nanoparticles of 4.3, 4.0 and 4.5 mass % in heat-treated WSRG with Fe_2O_3 content of 10, 30 and 50 mass %, respectively. These results are consistent with the conclusion that the visible light-

activated the photocatalytic effect of heat-treated WSRG is closely related to the precipitated amount of α -Fe₂O₃ nanoparticles [9].

As an Advanced Oxidation Process (AOP), the Fenton reaction and the light-accelerated Fenton reaction, commonly known as the photo-Fenton reaction, appear to be promising for practical industrial applications [10-13]. When Fenton reaction systems are irradiated with UV/Visible light, this can accelerate the rate of degradation of a wide variety of pollutants. This behaviour upon irradiation is due principally to the photochemical reduction from Fe^{III} to Fe^{II}. Advantages of the photo-Fenton reaction include producing an additional hydroxyl radical, the species responsible for the degradation of organic material, and regeneration of Fe^{II} by light with the decomposition of water. As a consequence, the amount of H₂O₂ needed to convert Fe^{III} to Fe^{II} is reduced [11]. The significant advantage of the Fenton process is that the reagent components are safe to handle and environmentally friendly. Highly complicated apparatus and pressurized systems are not required for the oxidation process, making it a feasible technology for upscaling directly from laboratory-scale to full-scale [12]. Above all, if sunlight is used, the photo-Fenton treatment is far cheaper than other available AOP's such as ozonization [13].

The photocatalytic activity of oxide semiconductors is commonly considered in terms of the effect of the band gap energy . The wide band gap of TiO₂ (3.2 eV) is one factor hampering improvements towards more efficient devices working under a wide range of solar energies [14]. Photocatalytic tests carried out in photodecomposition of dipropyl sulfide showed good correlation between the band gap energyand the photocatalytic activity for metallophthalocyanine complexes [15]. ZnO as a semiconductor photocatalyst has the same drawback [16, 17]. Mohamed and Barakat [17] synthesized ZnO-SiO₂ nanoparticles by a sol-gel technique. The samples were further modified by nanosized Pt from H₂PtCl₆ solution through photoassisted deposition (PAD) and impregnation (Img) routes. As a result, the band gap energy has been decreased from 3.40 eV for ZnO-SiO₂ to 3.25, 3.05 eV for Img: Pt-ZnO-SiO₂, and PAD: Pt-ZnO-SiO₂, respectively. Phenol degradation efficiency increased from 80 to 85 and 99.9%, with the ZnO/SiO₂, Img: Pt-ZnO-SiO₂, and PAD: Pt-ZnO-SiO₂ samples, respectively [17].

In this work, we investigate the relationship between the structure and photocatalytic ability of glass and glass-ceramic samples prepared by melt-quenching and subsequent heat treatment, from recycled waste-slag by means of X-ray diffraction (XRD), ^{57}Fe -Mössbauer spectroscopy, transmission electron microscopy (TEM) and ultraviolet-visible absorption spectroscopy (UV-VIS).

2- Experimental

2. 1. Sample preparation:

One kg of waste slag was collected on July 14th, 2015 at Tamagawa municipal domestic waste combustion plant (Maruko 2-33-1, Ohta-ward, Tokyo 146-092, Japan). The chemical composition of this slag was previously analysed and reported to be CaO (21.79 mass%); SiO₂ (23.32); Fe₂O₃ (11.45); Al₂O₃ (16.68); Na₂O (6.57) and other minor components (20.19) [9]. A series of glass and glass-ceramic samples with different Fe₂O₃ concentration, (11 mass %, 14, 30 and 50) were prepared by a melt-quench method using the above described pulverized slag named SF11 Original, with varying levels of addition of Fe₂O₃. The mixtures of SF11 Original and Fe₂O₃ were melted at 1400 °C for 1 h in a platinum crucible. Samples without Fe₂O₃ additions, and with Fe₂O₃ additions, to adjust total Fe₂O₃ content to 30% and 50% were obtained by quenching the base of the crucible in ice-cold water. These samples are named as SF11 Melted, SF30 Melted and SF50 Melted, respectively.

In order to evaluate the effect of impurities, simulated slag glass was prepared from the chemical reagent of the main components excluding the other minor components, named as RSF14 Melted. The prepared samples and their Fe₂O₃ additions are listed in Table 1. Reagent chemicals used were Na₂CO₃ (Wako 199-01585), CaCO₃ (Wako 030-00385), Fe₂O₃ (Wako 096-04825), Al₂O₃ (Wako 012-01965) and SiO₂ (Kanto Kagaku 37974-00), they were well mixed in an agate mortar before sample preparation. All prepared samples were also separated, and a fraction of each was subjected to heat treatment at 800 °C for 100 min.

2. 2. Characterization techniques:

Sample structures before and after heat treatment were characterized by ^{57}Fe Mössbauer spectroscopy, X-ray diffractometry (XRD), and transmission electron microscopy (TEM). ^{57}Fe Mössbauer spectra were measured using a constant acceleration spectrometer. A source of 925 MBq $^{57}\text{Co}(\text{Rh})$ was attached to an MVT-1000 transducer connected to a MDU-1200 drive unit. The drive unit was connected to a DFG-1200 digital function generator, then to an ORTEC 570 amplifier. Transmitted γ -rays through the sample were detected by a photomultiplier tube. The counts were amplified by an ORTEC 142 preamplifier. The applied voltage (2 kV) was obtained by using an ORTEC 556 High voltage power supply, and an ORTEC 570 amplifier. The amplified signals were monitored with a PC via an ORTEC EASY-MSC. Samples with weight = 40 mg were homogeneously dispersed in a circular sample holder with 10 mm diameter; inserted into the spectrometer; and measured until the total counts collected were greater than 10^6 . Isomer shifts were given relative to $\alpha\text{-Fe}$ as a reference. The Mösswinn 3.0i XP software was used to analyze the obtained spectra.

XRD patterns were recorded using a TKYD07-028, Rigaku diffractometer between $^{\circ}2\theta$ of 10 to 80, with precision and scan rates of 0.02 and 5 degrees / minute, respectively. Cu- K_{α} rays ($\lambda = 0.1541 \text{ nm}$) were generated with a monochromator under 50 kV and 300 mA. TEM images were obtained using a JEM-3200FS Field Emission Energy Filter Electron Microscope.

For the evaluation of photocatalytic properties, we used 40 mg of pulverized sample and 10 mL of methylene blue aqueous solution (MB_{aq}) with an initial concentration of $20 \mu\text{mol L}^{-1}$. An additional amount (0.36 ml) of Hydrogen peroxide (9.79 M) (Wako: 081-04215 30% mass/mass) was added to the MB solution. The concentration of H_2O_2 in this solution was 0.34 M. UV–Vis spectra of the MB solution before and after the photocatalytic reaction test were obtained from the absorbance of the peak at 665 nm. The light was emitted by a metal-halide lamp with output wavelength region from 420 to 750 nm, an output power of 100 W and an intensity of 6 mW cm^{-2} , with the distance between the

sample and the light source maintained at 20 cm, and a UV filter to remove UV light. All samples were also measured in the dark to investigate the effect of adsorption.

For the evaluation of photocatalytic properties using sun light irradiation, the UV light intensity was ca. 5 mW/cm² in Hachioji (longitude 139.24, altitude 35.62), and temperature was 27 – 29 °C.

Diffuse reflectance spectra (DRS) were recorded between the wavelength of 190 and 1500 nm using a UV-VIS spectrometer with an integrating sphere. Barium sulfate was used as a reference in the diffuse reflection measurements. Sampling pitch and slit-width were set at 1.0 nm and 20 nm, respectively.

3. Results and discussion

3.1. Structural characterization:

3.1.1 XRD patterns:

Fig. 1 shows the XRD patterns for all samples before and after heat treatment at 800°C for 100 minutes. Before heat treatment, samples SF11 Original, SF11 Melted and RSF14 Melted show halo patterns, confirming the amorphous structure of these samples, while samples SF30 Melted and SF50 Melted are not glasses but glass-ceramics. Sample SF30 Melted produces diffraction peaks ascribed to magnetite (Fe₃O₄, PDF No. 96-900-9769), while sample SF50 Melted produces higher intensity peaks assigned to magnetite (Fe₃O₄, PDF No. 96-900-5840) and hematite (Fe₂O₃, PDF No. 96-901-5066). These results indicate that homogenous glass can be obtained with iron oxide contents of < 30%, while samples containing > 30% of iron oxide or more are glass-ceramics where the crystalline phase/s can be detected.

After heat-treatment at 800 °C for 100 min, sample SF11 Original produces broad diffraction peaks attributed to Gehlenite (Al₂Ca₂SiO₇, PDF No. 96-100-0049) and

magnetite (Fe_3O_4 , PDF No.96-151-3305). Sample SF11 Melted shows diffraction peaks with higher intensity due to Esseneite ($\text{Al}_{1.34}\text{CaO}_{0.97}\text{Fe}_{0.61}\text{O}_6\text{Si}_{1.08}$, PDF No. 96-900-1042) and alpha-dicalcium silicate (Ca_2SiO_4 , PDF No. 96-154-6029). Sample RSF14 Melted shows more clear crystalline peaks attributed to (AlSiO_7 , PDF No. 96-154-0253) and magnetite (Fe_3O_4 , PDF No. 96-900-2330). Interestingly, sample SF30 Melted after heat treatment shows the same peaks of the magnetite phase at almost the same diffraction angle due to magnetite (Fe_3O_4 , PDF No. 96-900-7707). For sample SF50 Melted, the detected diffraction peaks were assigned to magnetite (Fe_3O_4 , PDF No. 96-101-1033) and hematite (Fe_2O_3 , PDF No. 96-901-5066). It was noticed that for sample SF50 Melted, the hematite phase increased in abundance due to oxidation during heat-treatment, while the magnetite phase decreased in abundance. These results are consistent with the obtained Mössbauer spectra.

3.1.2 Mössbauer spectra:

For RT Mössbauer spectroscopy, the spectra and parameters of all samples before and after heat-treatment are shown in Fig. 2 and Table 2, respectively. Before heat treatment, sample SF11 Original exhibits two doublets, one related to $\text{Fe}^{\text{II}} T_{\text{d}}$, the second is related to $\text{Fe}^{\text{III}} O_{\text{h}}$. Sample SF11 Melted shows one doublet related to $\text{Fe}^{\text{III}} T_{\text{d}}$. RSF14 Melted has one doublet related to $\text{Fe}^{\text{III}} T_{\text{d}}$. Increasing the iron content to 30% and 50% results in three sextets only for sample SF50 Melted, with one assigned as (magnetite + maghemite), the second as magnetite, and the third as hematite. It also shows a doublet attributed to $\text{Fe}^{\text{III}} T_{\text{d}}$. The sample SF30 Melted shows only one doublet, attributed to $\text{Fe}^{\text{III}} O_{\text{h}}$.

After heat-treatment, all samples except for sample SF50 Melted show doublets with $\delta = (0.18 \pm 0.01) - (0.38 \pm 0.01 \text{ mm s}^{-1})$. Only sample SF11 Original has an additional doublet due to $\text{Fe}^{\text{II}} O_{\text{h}}$ with a small spectral area (and hence abundance) of 9.8%. Sample SF50 Melted produces a doublet related to $\text{Fe}^{\text{III}} T_{\text{d}}$ and two sextets due to hematite and

maghemite. The increase in the hematite component for sample SF50 Melted from 9.8% before heat treatment to 38.1% after heat treatment matches the XRD measurements.

The best performing samples for the photo-Fenton reaction were samples RSF14 Melted and SF11 Melted. The room temperature Mössbauer spectra for those samples show no magnetic components, so the heat treated samples were measured at 77 K to provide further investigation. The spectra and fitted parameters are shown in Fig. 3 and Table 3, respectively. It can be seen that for samples SF11 Original, SF11 Melted and RSF14 Melted, no magnetic components are detected. Unlike the room temperature spectra, for sample SF30 Melted, one doublet arises from $\text{Fe}^{\text{III}} T_{\text{d}}$ and three sextets arise from (maghemite + magnetite), hematite, and magnetite, respectively. Sample SF50 Melted produces two sextets (one due to hematite and one to maghemite), and one doublet due to $\text{Fe}^{\text{III}} T_{\text{d}}$.

3.1.3 TEM Images:

TEM images for the heat-treated samples are shown in Fig. 4. The SF11 Original sample is mostly amorphous (see XRD pattern). Sample SF11 Melted has nanoparticles with a size of ca. 10 nm and crystalline structure can be seen at high magnification. Sample RSF14 Melted shows a crystalline structure and nanoparticle sizes varying from 10 - 70 nm. For sample SF30 Melted, nanoparticles with size varying from 20 - 30 nm were detected, while for sample SF50 Melted no nanostructure can be observed, even with very high magnification. These results confirm the precipitation of iron nanoparticles during melting at 1400 °C and / or quenching; and that the size of the nanoparticles is broadly correlated to the iron content of the sample.

3.2. Photocatalytic activity measurements:

Fig. 5 (dotted lines) shows the pseudo-first-order rate constant (k) of MB decomposition in the presence of the different samples after heat-treatment. The best-performing samples

were SF30 Melted and SF50 Melted, both with $k = (3.00 \pm 0.08) \times 10^{-3} \text{ min}^{-1}$. These samples have the highest iron oxide contents. The samples SF11 Original and SF11 Melted also have the same *k-value* of $(2.30 \pm 0.06) \times 10^{-3} \text{ min}^{-1}$, this is mostly due to the similarity in structure. The sample RSF14 Melted has the lowest *k-value* of $(1.80 \pm 0.05) \times 10^{-3} \text{ min}^{-1}$.

To investigate the similarity in structure, diffuse reflectance spectroscopy (DRS) was used to measure the band gap for all samples after heat treatment. The degradation of blank (MB solution without catalyst) and dark samples (MB and catalyst without visible light irradiation) were measured. For these measurements, the pseudo-first-order rate constant (k) of MB decomposition was small compared to the irradiated samples, with $k = (0.70 \pm 0.02)$ and $(0.20 \pm 0.01) \times 10^{-3} \text{ min}^{-1}$, respectively. All samples were also measured before heat treatment, providing a maximum *k-value* of $(1.00 \pm 0.03) \times 10^{-3} \text{ min}^{-1}$.

DRS measurements:

The bandgap energies of the heat-treated samples were measured using diffuse reflectance spectroscopy. The band gap energy (E_g) was estimated using the following equation, a Tauc plot [18]:

$$(h\nu\alpha)^{1/n} = A(h\nu - E_g) \quad (1)$$

where h , ν , α , n and A are Plank's constant, frequency of light, absorption coefficient, n is a number that characterizes the transition process, in this case ($n = 0.5$) and A is the proportionality factor. Fig. 6 shows the Tauc plot used to calculate the band gap; the E_g values are listed in Table 1. The calculated band gap energy for sample SF11 Original is $(2.15 \pm 0.02 \text{ eV})$ which is near to the band gap energy of sample SF11 Melted $(2.09 \pm 0.02 \text{ eV})$. For sample RSF14 Melted E_g was the highest obtained, at $2.22 \pm 0.04 \text{ eV}$, which

explains why it has the lowest *k-value* of the studied samples. Samples SF30 Melted and SF50 Melted have the same band gap energy (1.96 ± 0.01 eV). Despite the differences in hematite content of these samples, both have the same *k-value* of 3×10^{-3} min⁻¹. This can be attributed to the differences in sizes of precipitated nanoparticles..

3.3. Enhancement of the photoactivity by the photo-Fenton reaction.

With the aim of obtaining enhanced performance, the photo-Fenton reaction has been applied. Hydrogen peroxide was added to 10 ml of MB solution; the concentration of H₂O₂ in this solution was 0.34 M. As a result, higher *k-value*s were obtained: up to $(2.8 \pm 0.08) \times 10^{-2}$ min⁻¹ and $(2.2 \pm 0.07) \times 10^{-2}$ min⁻¹ for samples RSF14 Melted and SF11 Melted, respectively. Fig. 5 (solid lines) shows the pseudo-first-order rate constant of MB decomposition for all samples with the photo-Fenton experiment and associated *k*-values. It is noted that applying the photo-Fenton reaction halves the maximum degradation time, from 6 to 3 hours. This enhancement is mainly due to the photochemical reduction of Fe^{III} to Fe^{II}, and thus more Fe^{II} will be available to react with H₂O₂ [11].

Brahmia reported that TiO₂ can be used for MB degradation under UV light with *k-value* of 33×10^{-3} min⁻¹[19]. The TiO₂ polyacrylamide (TiO₂/PAAm) hydrogel was used to remove MB from aqueous solution. Those results showed that about 95% of a 10 mg/L MB solution was photocatalytically degraded after 5 h under sunlight irradiation [20]. A TiO₂ sol was prepared for the degradation of methylene blue (MB) solution under ultraviolet irradiation where the performance of 92.3% for colour removal was achieved after 160 min [21]. By comparison with the results we have obtained here,, it can be concluded that the prepared samples from slag can be a promising candidate as low-cost photocatalyst materials.

This work aims to prepare a catalyst with high degradation capability and low cost which can potentially be applied for wastewater treatment, so the sample SF11 Melted has been chosen for further study as it is simply melted slag with no need to add iron oxide, and the photo-Fenton reaction has been applied to this sample for the next investigation.

3.4. Parameters affecting the photocatalytic activity.

3.4.1. Catalyst Photoactivity under solar light irradiation:

Using direct solar light is favourable for practical applications. Here, MB degradation under solar light irradiation was measured. The results, shown in Fig. 7, indicate an increase in k -value from (1.6 ± 0.05) , (2.2 ± 0.07) and (3.4 ± 0.1) to (3.5 ± 0.2) , (4.4 ± 0.2) and $(6.2 \pm 0.3) \times 10^{-2} \text{ min}^{-1}$ for catalyst loading of $(2, 4$ and $8 \text{ g / L})$, respectively. The obtained k -values in sunlight are almost double their values obtained using an irradiation source. This enhancement can be attributed to the existence of UV light in the solar spectrum which is not provided by the irradiation source, since a UV filter was placed in front of the irradiation source lamp [22].

3.4.2. Effect of catalyst loading:

One of the advantages of these catalysts is that the catalyst amount can be increased to a high value (due to high abundance and low cost), leading to an increase in degradation efficiency. In our case, the catalyst loading was varied from 2 to 64 g / L . The results of the degradation values as a function of catalyst loading are presented in Fig. 8. These show that the MB degradation, measured at 30 min , increases with catalyst loading from $(24.0 \pm 0.5) \%$ for 2 g / L to $(97 \pm 2) \%$ for 32 g / L . The increase in the degradation was due to the increase in the number of active surfaces on the catalyst per unit volume of MB [23], with an increase in the absorbed photons by the catalyst [24]. However, at 64 g / L , the degradation decreases: this is attributed to reductions in light which can reach to the catalyst as the solution opacity increases [25]. The optimum catalyst loading was found to be 32 g / L .

3.4.3. The effect of initial dye concentration:

To investigate the effects of dye concentration, the *k*-values were measured at different dye concentrations of 20, 40 and 60 μM , and also at different catalyst loading levels simultaneously Fig. 9. It was found that, as the dye concentration increases, the *k*-value decreases; this is due to decreasing light penetrating the dye solution and reaching the catalyst as the solution gets darker and thus the formation of hydroxyl radicals is decreased since the dye molecules occupy the active sites of the catalyst [24, 20].

3.4.4. The effect of solution temperature:

The degradation of MB solution at different temperatures of 30, 40, 50 and 60 $^{\circ}\text{C}$ was measured after 30 min of irradiation. The degradation at these temperatures was (37 ± 2) , (44 ± 3) , (74 ± 4) and (94 ± 6) %, respectively. Although the degradation increases as the temperature increases, this is due to the high temperature rather than changes in photoactivity, as shown in Fig. 10. The degradation in the dark and blank samples also increased, especially at high temperature. The increase in degradation caused directly by temperature is due to increased mobility of hydroxyl radicals, leading to faster reaction with the dye molecules since the electron-hole pair recombination decreases [24, 25]. The same behaviour was observed by Mozia et al., in the case of azo dye Acid Red 18 [26], the degradation for blank or dark samples were not reported.

3.4.5. Effect of H_2O_2 dosage:

The concentration of H_2O_2 in MB solution was studied in the range from 0.08 to 0.68 M; the results are shown in Fig. 11. The highest *k*-value $2.8 \times 10^{-2} \text{ min}^{-1}$ was obtained with H_2O_2 dosage of 0.17 M. The enhancement of the degradation with increasing H_2O_2 dosage is due to increased generation of hydroxyl radicals. Above 0.17 M, degradation decreases due to the excess H_2O_2 encouraging $(\text{HO}^{\bullet})_2$ production and lowering $\cdot\text{OH}$ generation. It is also reported that excess of H_2O_2 could generate $\cdot\text{OH}$, which can dimerize to form H_2O_2 , so this cumulative effect inhibits degradation [23].

3. 5. Catalyst stability:

The SF11 Melted and RSF14 Melted samples were reused under the same conditions for 7 times Fig. 12 with no cleaning or treatment of any kind in between subsequent experiments. The degradation was found to decrease by 5 and 15%, respectively, which is a promising result for reusing these catalyst materials, potentially leading to lower costs. It is important that these repeated measurements were carried out by simply centrifuging the solution then removing and replacing it with a new MB solution. No further filtration or drying of the powder was carried out, which is considered an advantage for easy and practical reusing.

Conclusions

Slag-derived glass and glass-ceramic samples were successfully prepared by a melt-quench method, characterised, and then used as a photocatalytic material to decompose methylene blue dye under visible light and solar light irradiation. The photocatalytic activity of the prepared samples was found to obey the pseudo-first-order rate constant, having a k -value of $3 \times 10^{-3} \text{ min}^{-1}$ for the samples SF30 Melted and SF50 Melted. In the photo-Fenton process, the k -values increased to $2.8 \times 10^{-2} \text{ min}^{-1}$ and $2.2 \times 10^{-2} \text{ min}^{-1}$ for the samples RSF14 Melted and SF11 Melted, respectively.

Irradiating sample SF11 Melted with direct solar light doubles the k -values up to $4.4 \times 10^{-2} \text{ min}^{-1}$. There is good correlation between the photocatalytic activity and the precipitated amount of hematite, while in the case of the photo-Fenton reaction, the degradation is mainly caused by paramagnetic iron Fe^{III} oxide. The optimum conditions for practical usage of the samples are using SF11 Melted sample in photo-Fenton reaction with 0.17 M of H₂O₂ in sunlight with a maximum catalyst loading 32 g / L.

Acknowledgments

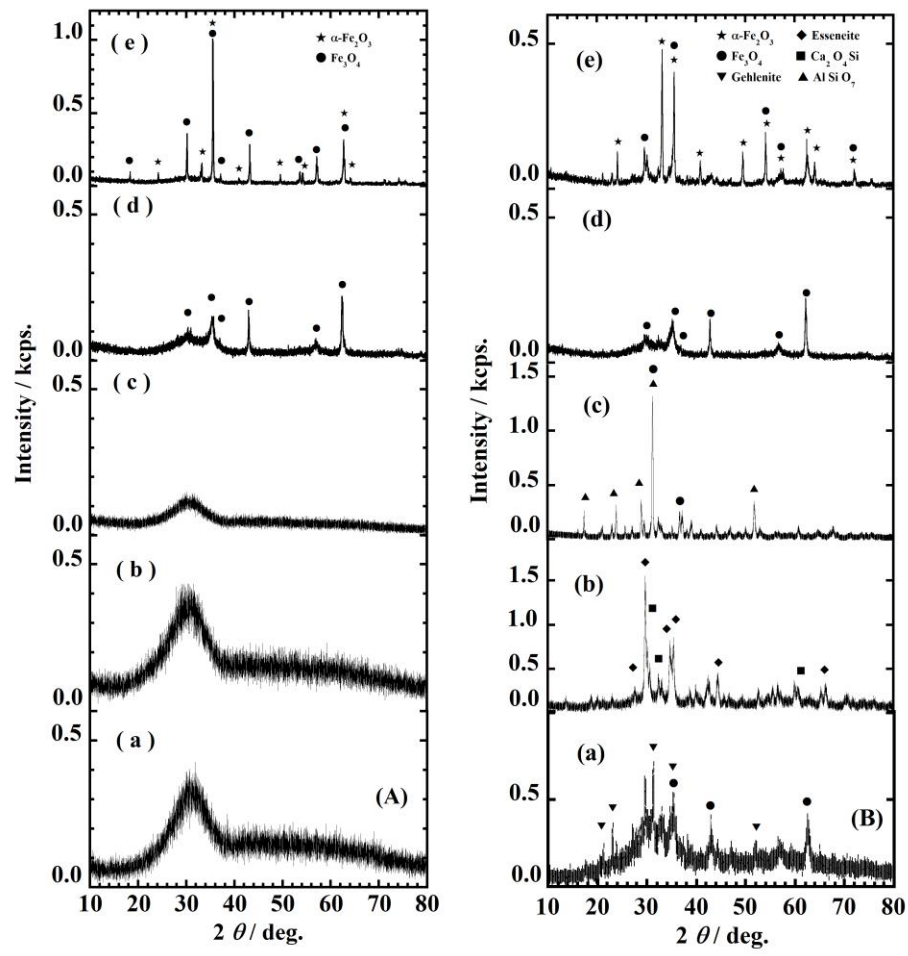
Some of the authors (ASA, KN, SK) express their gratitude for the financial support from Tokyo Human Resources Fund for City Diplomacy.

References

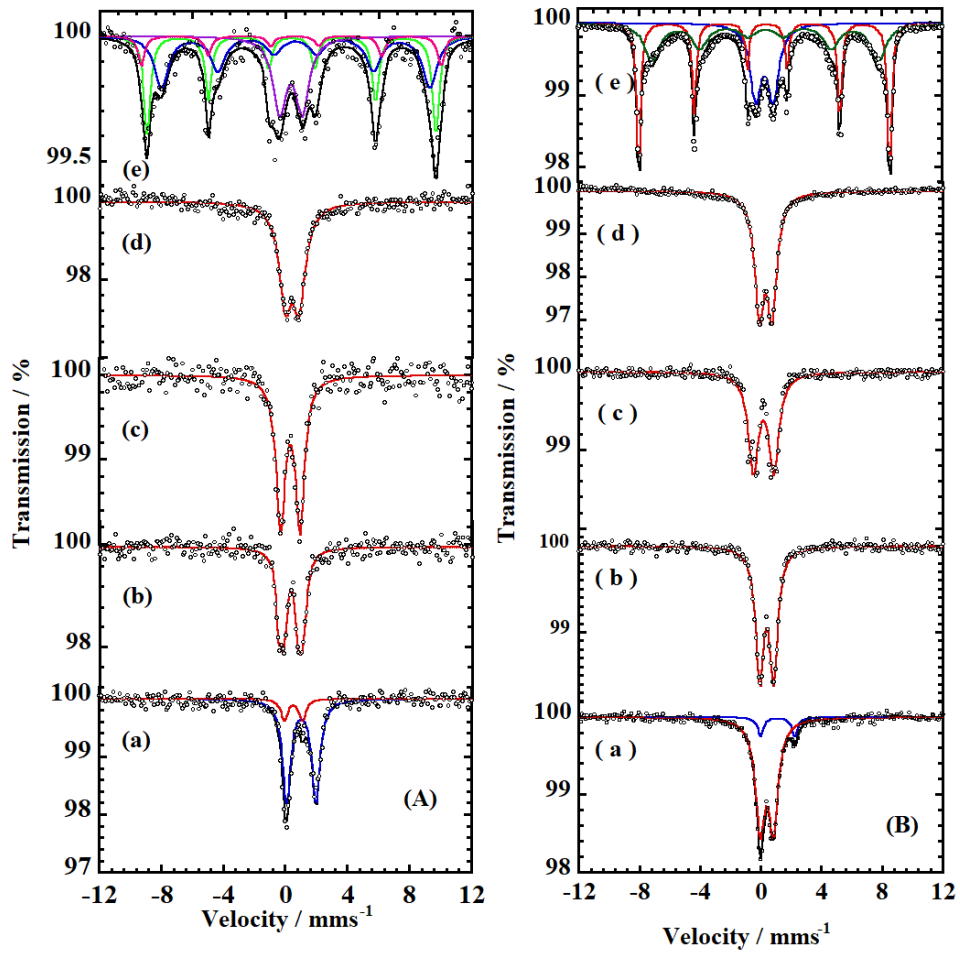
- [1] OECD (2016), OECD Factbook 2015-2016: Economic, Environmental and Social Statistics, OECD Publishing, Paris. <http://dx.doi.org/10.1787/factbook-2015-en>.
- [2] Waste report, Clean Authority of TOKYO (2017) <http://www.union.tokyo23-seisou.lg.jp/seiso/seiso/pamphlet/report/documents/gomirepoepdf.pdf>. Accessed 1 Jan 2019
- [3] Fujishima A, Honda K (1972) Electrochemical Photolysis of Water at a Semiconductor Electrode. *Nature*. 238:37-38
- [4] Chang W, Zhang M, Rena X and Miller A (2017) Synthesis and Photocatalytic Activity of Monolithic Fe₂O₃/TiO₂. *S. Afr. J. Chem.* 70:127-131
- [5] Kubuki S, Iwanuma J, Takahashi Y, Akiyama K, Homonnay Z, Sinkó K, Kuzmann E, Nishida T (2014) Visible light activated catalytic effect of iron containing soda-lime silicate glass characterized by ⁵⁷Fe-Mössbauer spectroscopy. *J. Radioanal. Nucl. Chem.* 301:1-7
- [6] Iida Y, Akiyama K, Kobzi B, Sinkó K, Homonnay Z, Kuzmann E, Ristić M, Krehula S, Nishida T, Kubuki S (2015) Structural analysis and visible light-activated photocatalytic activity of iron-containing soda lime aluminosilicate glass. *J. Alloys. Comp.* 645:1-6
- [7] Kubuki S, Iwanuma J, Akiyama K, Homonnay Z, Kuzmann E, Nishida T (2013) Water cleaning ability and local structure of iron-containing soda-lime silicate glass. *Hyperfine Interact.* 218:41-45
- [8] Kubuki S, Nishida T (2013) In: Sharma V. K, Klingelhofer G, Nishida T (Eds.) Mössbauer Spectroscopy: Applications in Chemistry, Biology, Nanotechnology, Industry and Environment, 1st edn. Wiley & Sons, Hoboken, NJ, USA
- [9] Ishikawa S, Kobzi B, Sunakawa K, Nemeth S, Lengyel A, Kuzmann E, Homonnay Z, Nishida T, Kubuki S (2017) Visible-light activated photocatalytic effect of glass and glass-ceramic prepared by recycling waste slag with hematite. *Pure Appl Chem* 89(4):535-554
- [10] Aramyan S and Moussavi M (2017) Advances in Fenton and Fenton Based Oxidation Processes for Industrial Effluent Contaminants Control-A Review. *Int J Environ Sci Nat Res*, 2:1-18

- [11] Machulek A, Quina F, Gozzi F, Silva V, Friedrich L and Moraes J (2012) In: Tomasz Puzyn (ed.) *Organic Pollutants Ten Years After the Stockholm Convention - Environmental and Analytical Update*, 1st edn. Intechopen, London, UK
- [12] Kavitha V, Palanivelu K (2004) The role of ferrous ion in Fenton and photo-Fenton processes for the degradation of phenol. *Chemosphere*. 55:1235-1243
- [13] Bauer R, Fallmann H (1997) The Photo-Fenton Oxidation - A cheap and efficient wastewater treatment method. *Res. Chem. Intermed.* 23:341-354
- [14] Gharaei S , Abbasnejad M and Maezono R (2018) Band gap reduction of photocatalytic TiO₂ nanotube by Cu doping. *Nature Research* 8, 14192 (2018)
- [15] Cojocaru B, Neațu S, Pârvulescu V, Dumbuya K, Steinrück H, Gottfried J, Aprile C, Garcia H and Scaiano J (2009) Band gap effect on the photocatalytic activity of supramolecular structures obtained by entrapping photosensitizers in different inorganic supports. *RCS* 11:5569-5577
- [16] Hunge Y and Yadav A (2018) Basics and advanced developments in photocatalysis – a review. *Int J Hydro*.2:539-541
- [17] Mohamed R and Barakat M (2012) Enhancement of Photocatalytic Activity of ZnO/SiO₂ by Nanosized Pt for Photocatalytic Degradation of Phenol in Wastewater. *International Journal of Photoenergy* 2012:1-8
- [18] Tauc J, Grigorovici R and Vancu A (1966) Optical Properties and Electronic Structure of Amorphous Germanium. *Phys. Status Solid.* 15:627-637
- [19] Brahmia Q, (2016) Photocatalytic Degradation of a Textile Dye under UV and Solar Light Irradiation Using TiO₂ and ZnO nanoparticles. *IJACEBS* 3:225-227
- [20] Kazemi F, Mohamadnia Z, Kaboudin B, Karimi Z (2016) Photodegradation of methylene blue with a titanium dioxide/polyacrylamide photocatalyst under sunlight. *J. APPL. POLYM. SCI.* 43386:1-9
- [21] Yao J and Wang C, (2010) Decolorization of Methylene Blue with TiO₂ Sol via UV Irradiation Photocatalytic Degradation. *International Journal of Photoenergy* 2010:1-6

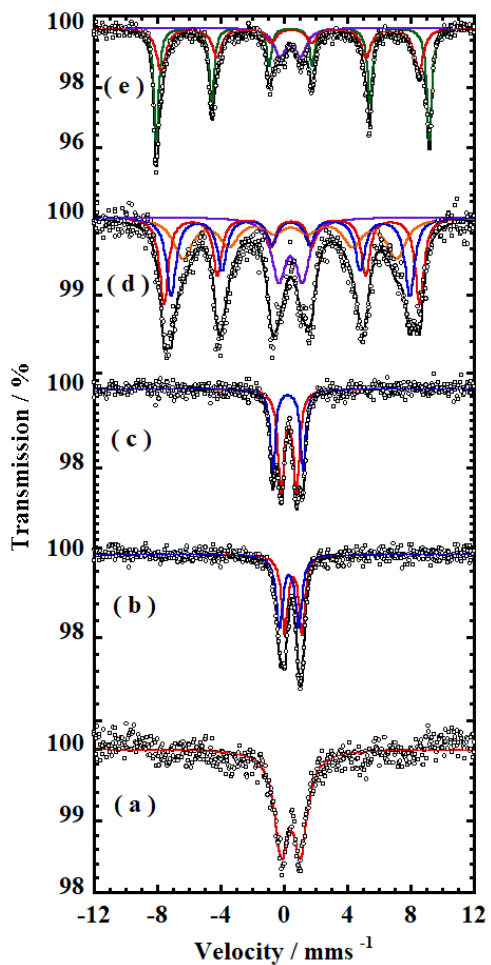
- [22] Hu Q, Liu B, Zhang Z, Song M, Zhao X (2010) Temperature Effect on the Photocatalytic Degradation of Methyl Orange under UV-vis Light Irradiation. Wuhan University of Technology and Springer-Verlag Berlin Heidelberg, 25:209-213
- [23] Nasuha N, Ismail S, Hameed B.H (2017) Activated electric arc furnace slag as an effective and reusable Fenton-like catalyst for the photodegradation of methylene blue and acid blue 29. J.Jenvman, 196:323-329
- [24] Khan R, ASW Kurny, Fahmida G (2017) Parameters affecting the photocatalytic degradation of dyes using TiO₂: a review. Appl Water Sci 7:1569
- [25] Susheela Bai G (2012) Photocatalytic Degradation Study of Methylene Blue Solutions and Its Application to Dye Industry Effluent. IJMER 2:1204-1208
- [26] Mozia S, Morawski A, Toyoda M, Inagaki M (2009) Application of anatase-phase TiO₂ for decomposition of azo dye in a photocatalytic membrane reactor. Desalination, 24:97105



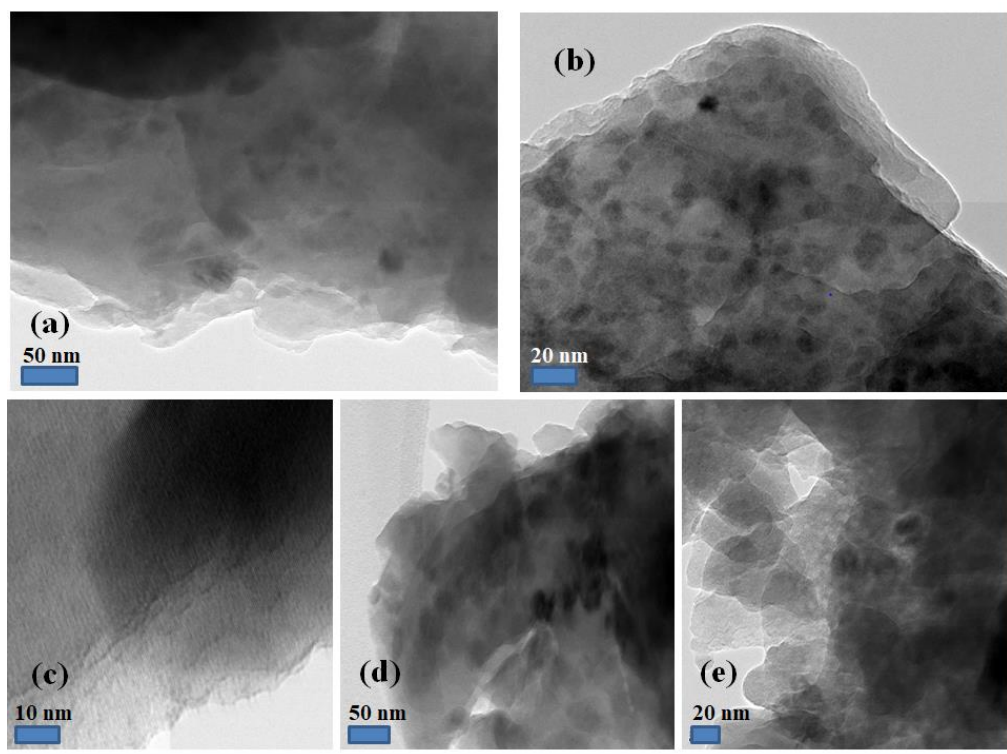
A. S. Ali *et al.*, Fig. 1 (A), (B)



A. S. Ali *et al.*, Fig. 2 (A), (B)

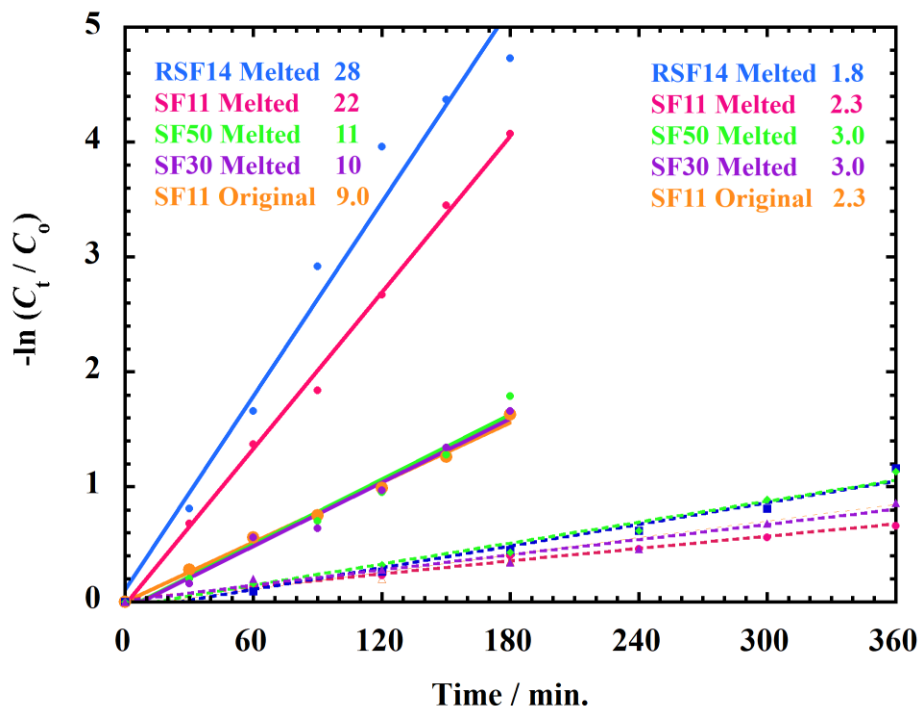


1
2
3
4
5
6
7
8
9
10 A. S. Ali *et al.*, Fig. 3
11



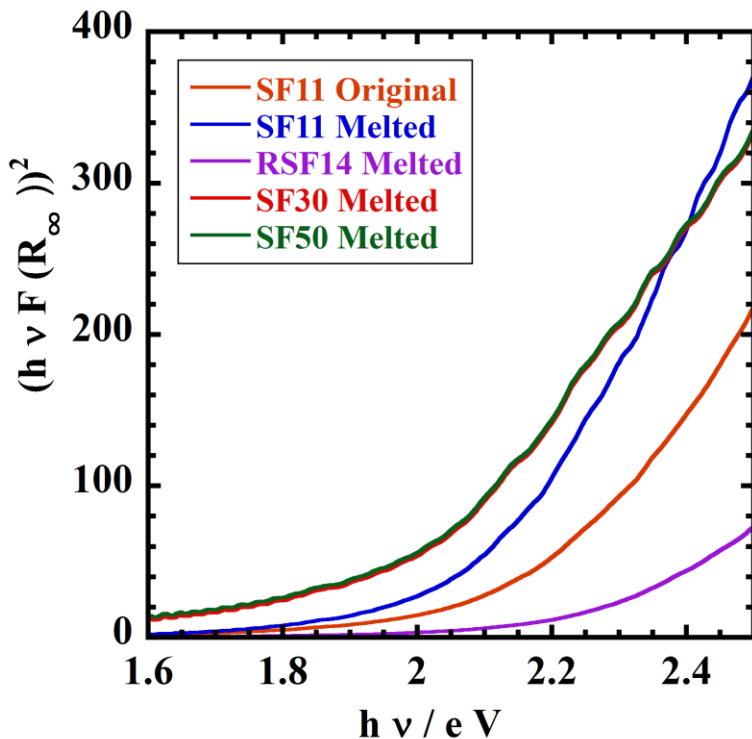
12
13
14
15
16
17
18
19
20
21
22
23

A. S. Ali *et al.*, Fig. 4



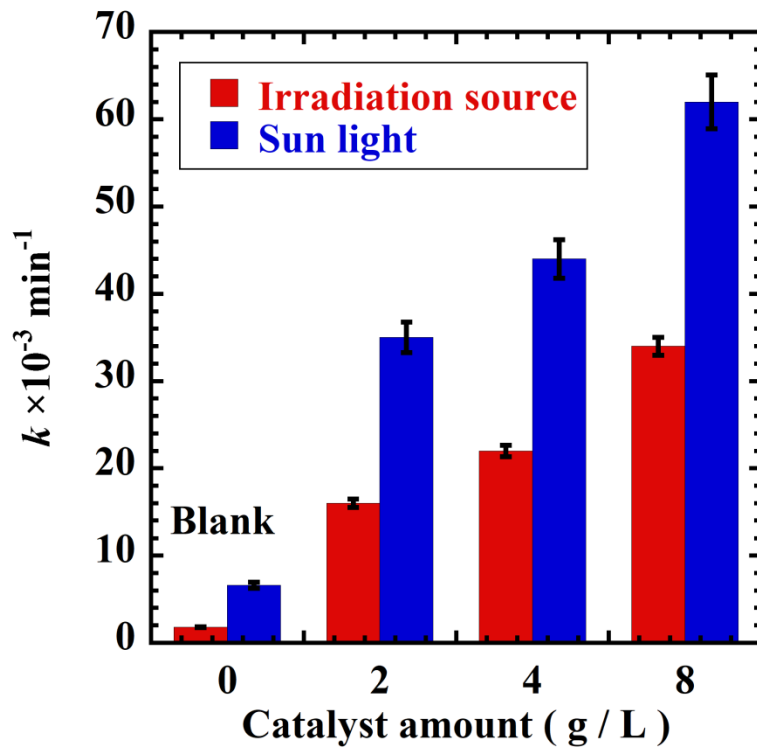
24
25
26
27
28
29
30
31
32
33
34
35
36
37 A. S. Ali *et al.*, Fig. 5

38
39
40
41
42
43
44
45
46
47
48
49
50

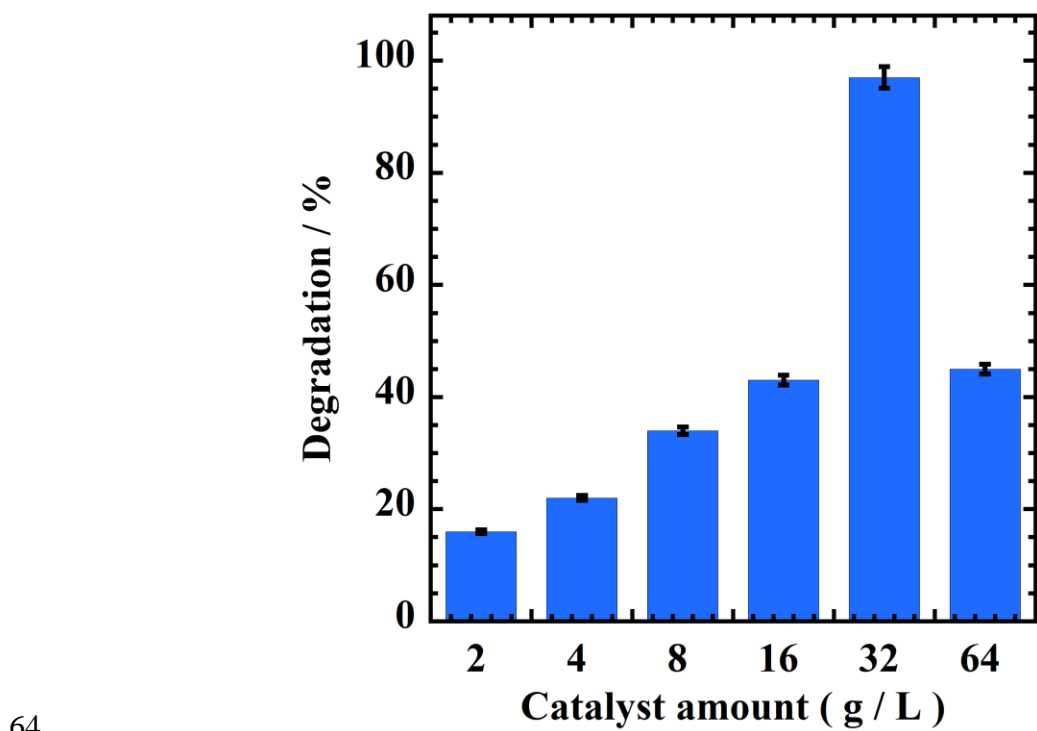


A. S. Ali *et al.*, Fig. 6

51
52
53
54
55
56
57
58
59
60
61
62
63

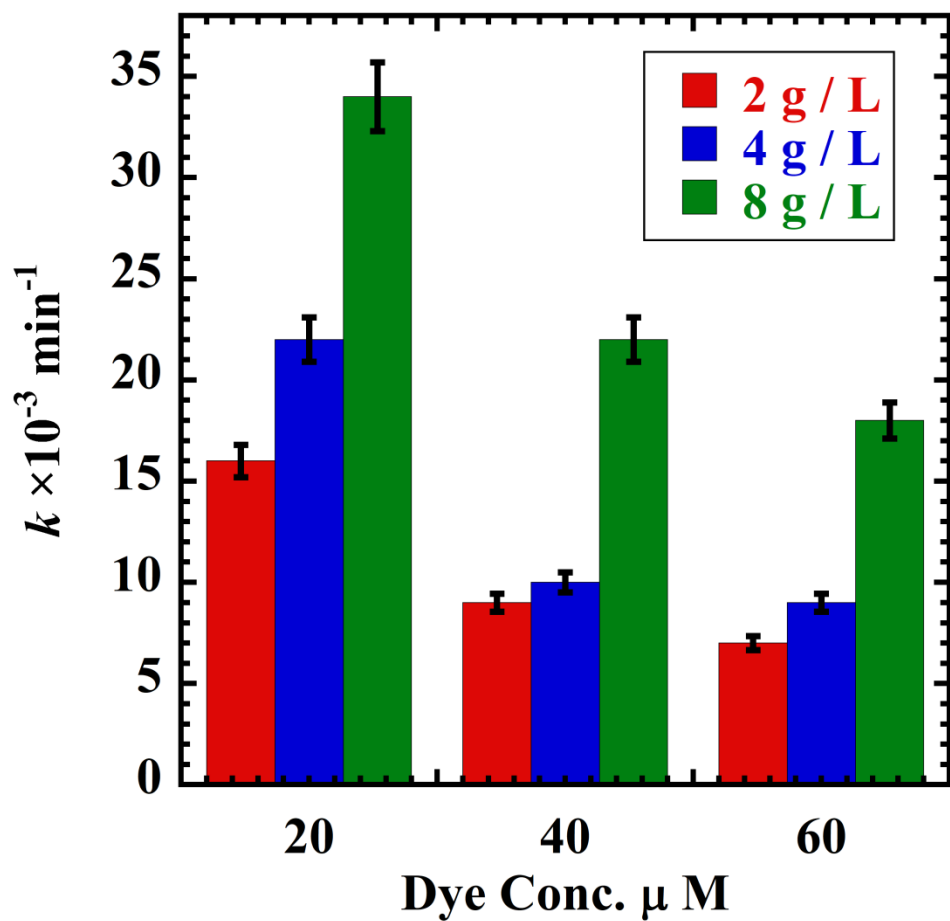


A. S. Ali *et al.*, Fig. 7

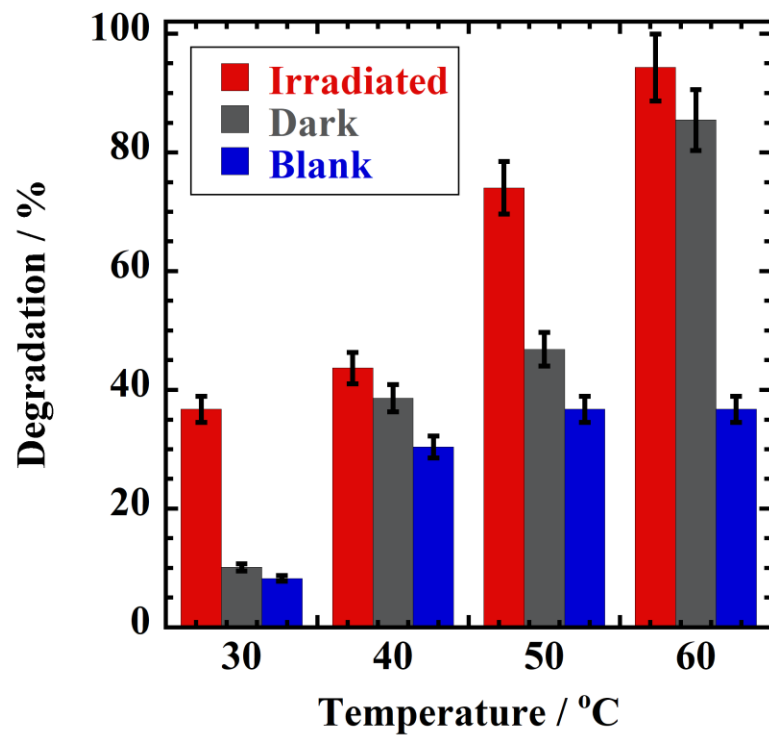


64
65
66
67
68
69
70
71
72
73
74
75
76

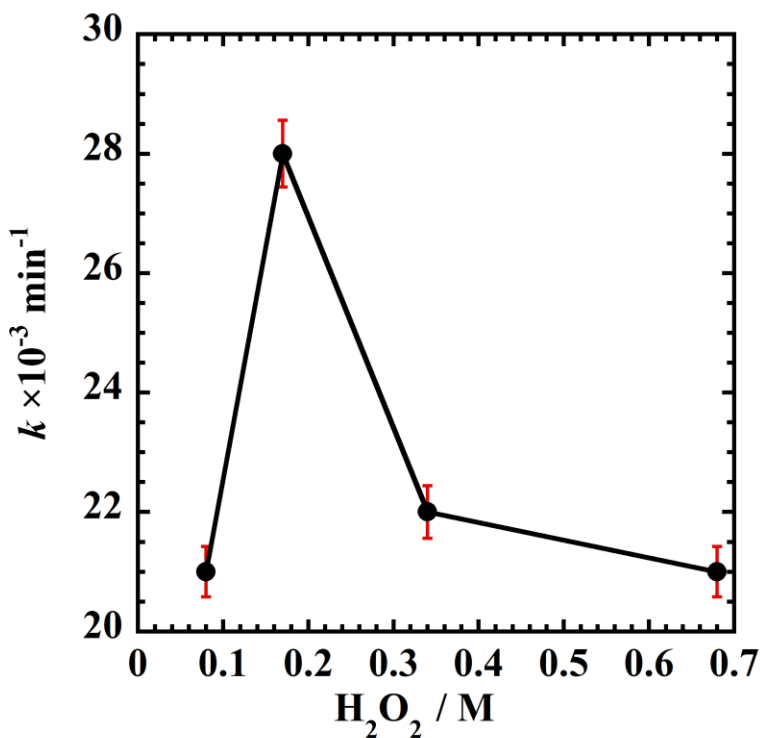
A. S. Ali *et al.*, Fig. 8



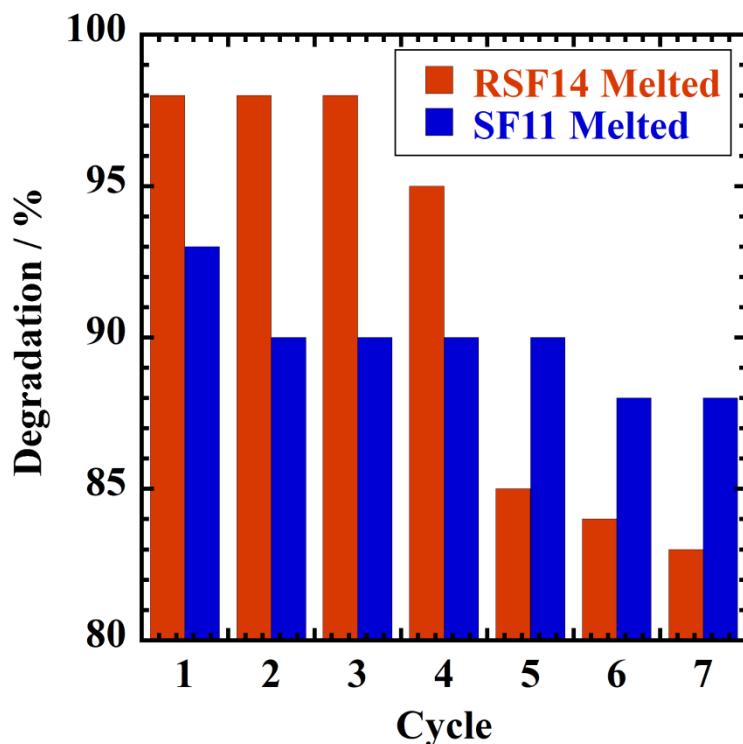
77
78
79
80
81
82
83
84
85
86
87 A. S. Ali *et al.*, Fig. 9



88
89
90
91
92
93
94
95
96
97
98
99
100 A. S. Ali *et al.*, Fig. 10



101
102
103
104
105
106
107
108
109
110
111
112
113 A. S. Ali *et al.*, Fig. 11



114

115

116

117

118

119

120

121

122

123

124

125

126 A. S. Ali *et al.*, Fig. 12

127

128

129 Figure Captions

130 **Fig. 1** XRD patterns of slag samples (A) before and (B) after heat treatment at 800 °C for
131 100 min of (a) SF11 Original, (b) SF11 Melted, (c) RSF14 Melted, (d) SF30 Melted and
132 (e) SF50 Melted

133

134 **Fig. 2** RT Mössbauer of slag samples (A) before and (B) after heat treatment at 800 °C
135 for 100 min of (a) SF11 Original, (b) SF11 Melted, (c) RSF14 Melted, (d) SF30 Melted
136 and (e) SF50 Melted

137
138 **Fig. 3** Mössbauer spectra measured at 77 K of slag samples after heat treatment at 800
139 °C for 100 min; (a) SF11 Original, (b) SF11 Melted, (c) RSF14 Melted, (d) SF30 Melted,
140 (e) SF50 Melted

141
142 **Fig. 4** TEM images of slag samples of (a) SF11 Original, (b) SF11 Melted, (c) RSF14
143 Melted, (d) SF30 Melted, (e) SF50 Melted after heat treatment at 800 °C for 100 min

144
145 **Fig. 5** Kinetic dye degradation measurements of methylene blue for slag samples heat
146 treated at 800 °C for 100 min solid lines is under photo Fenton and dotted lines under
147 visible light

148
149 **Fig. 6** Tauc's plot for slag samples heat treated at 800 °C for 100 min

150
151 **Fig. 7** k values for SF11 Melted heat treated at 800 °C for 100 min using vis. light
152 irradiation source (in red) and sunlight (in blue)

153
154 **Fig. 8** Effect of catalyst loading on the MB degradation for the sample SF11 Melted heat
155 treated at 800 °C for 100 min

156
157 **Fig. 9** Effect of initial dye concentration on the MB degradation for the sample SF11
158 Melted heat treated at 800 °C for 100 min

159
160 **Fig. 10** Effect of temperature on the MB degradation of the sample SF11 Melted heat
161 treated at 800 °C for 100 min

163 **Fig. 11** Effect of H₂O₂ concentration on MB degradation of the sample SF11 Melted heat
164 treated at 800 °C for 100 min with catalyst loading 4 g / L and MB conc. of 20 µM

165
166 **Fig. 12** Reuse measurements of the samples SF11 Melted and RSF14 Melted heat treated
167 at 800 °C for 100 min

168

169

170

171

172

173

174

175

176

177

178

179

180

181

182

183

184 **Table 1** Fe₂O₃ (batch) content and bandgap energy of heat-treated slag samples
185 calculated from DRS

Sample	Total Fe ₂ O ₃ content (mass %)	E _g (eV)
SF11 Original	11.45 ± 0.01	2.15 ± 0.02
SF11 Melted	11.45 ± 0.01	2.09 ± 0.02
RSF14 Melted	14.40 ± 0.01	2.22 ± 0.04
SF30 Melted	30.00 ± 0.01	1.96 ± 0.01
SF50 Melted	50.00 ± 0.01	1.96 ± 0.01

186
187
188
189

190

191

192

193

194

195

196

197

198
199
200
201
202

203 A. S. Ali *et al*

204 **Table 2** ^{57}Fe -Mössbauer parameters at room temperature of slag glass samples before and
 205 after heat treatment at 800 °C for 100 min

	Sample	assignment	A (%)	δ (mm s ⁻¹)	Δ (mm s ⁻¹)	H_{int} (T)	Γ (mm s ⁻¹)
Before	SF50 Melted	mag + mgh	32.2	0.30 ± 0.01	-0.02 ± 0.02	48.10 ± 0.01	0.42 ± 0.03
		mag.	34.4	0.52 ± 0.02	0.00	44.80 ± 0.02	0.88 ± 0.10
		$\text{Fe}^{\text{III}} T_{\text{d}}$	23.6	0.27 ± 0.02	1.21 ± 0.03	-	0.84 ± 0.05
		hem.	9.8	0.37 ± 0.03	-0.20 ± 0.01	49.96 ± 0.02	0.43 ± 0.04
	SF30 Melted	$\text{Fe}^{\text{III}} O_{\text{h}}$	100.0	0.40 ± 0.01	0.89 ± 0.02	-	0.99 ± 0.03
		$\text{Fe}^{\text{III}} T_{\text{d}}$	100.0	0.31 ± 0.01	1.25 ± 0.02	-	0.69 ± 0.02
	SF11 Melted	$\text{Fe}^{\text{III}} T_{\text{d}}$	100.0	0.33 ± 0.01	1.25 ± 0.01	-	0.69 ± 0.02
		$\text{Fe}^{\text{II}} T_{\text{d}}$ $\text{Fe}^{\text{III}} O_{\text{h}}$	85.5	1.00 ± 0.01	1.89 ± 0.02	-	0.63 ± 0.02
	After		14.5	0.50 ± 0.02	1.16 ± 0.08	-	0.51 ± 0.10
	SF50 Melted	$\text{Fe}^{\text{III}} T_{\text{d}}$	25.5	0.31 ± 0.03	1.14 ± 0.01	-	
		hem.	38.1	0.37 ± 0.01	-0.18 ± 0.04	51.40 ± 0.01	
		mgh.	36.4	0.37 ± 0.01	-0.02 ± 0.01	46.40 ± 0.01	
	SF30 Melted	$\text{Fe}^{\text{III}} T_{\text{d}}$	100.0	0.32 ± 0.02	0.84 ± 0.03	-	
		$\text{Fe}^{\text{III}} T_{\text{d}}$	100.0	0.18 ± 0.01	1.34 ± 0.01	-	
	SF11 Melted	$\text{Fe}^{\text{III}} O_{\text{h}}$	100.0	0.38 ± 0.04	0.92 ± 0.01	-	
		$\text{Fe}^{\text{II}} O_{\text{h}}$	9.8	1.10 ± 0.02	2.25 ± 0.05	-	
	Original	$\text{Fe}^{\text{III}} O_{\text{h}}$	90.2	0.37 ± 0.01	0.88 ± 0.01	-	
						0.75 ± 0.01	

206 hem.: Hematite, mag.: Magnetite, mgh.: Maghemite, T_{d} : Tetrahedra, O_{h} : Octahedra, A: Absorption area,

207 δ : Isomer shift, Δ : Quadrupole splitting, H_{int} : Internal magnetic field, Γ : Line width.

208 **Table 3** ^{57}Fe -Mössbauer parameters at 77 K of slag samples heat-treated at 800 °C for
 209 100 min

sample	assignment	A (%)	δ (mm s ⁻¹)	Δ (mm s ⁻¹)	H_{int} (T)	Γ (mm s ⁻¹)
SF50 Melted	Fe ^{III} T_d	14.1	0.40 \pm 0.02	1.31 \pm 0.03	-	0.92 \pm 0.05
	hem.	49.0	0.48 \pm 0.01	0.13 \pm 0.01	53.50 \pm 0.01	0.37 \pm 0.01
	mgh.	36.9	0.43 \pm 0.01	-0.11 \pm 0.01	50.40 \pm 0.08	0.71 \pm 0.02
SF30 Melted	Fe ^{III} T_d	15.6	0.41 \pm 0.02	1.50 \pm 0.03	-	1.05 \pm 0.05
	Mag + mgh	27.9	0.40 \pm 0.03	-0.08 \pm 0.05	41.90 \pm 0.40	1.40 \pm 0.10
	hem.	28.1	0.48 \pm 0.01	0.01 \pm 0.01	50.20 \pm 0.10	0.65 \pm 0.04
	mag.	28.4	0.42 \pm 0.01	-0.04 \pm 0.02	46.80 \pm 0.10	0.73 \pm 0.07
RSF14 Melted	Fe ^{III} T_d	58.5	0.29 \pm 0.01	0.96 \pm 0.01	-	0.46 \pm 0.01
	Fe ^{III} T_d	41.5	0.24 \pm 0.01	1.90 \pm 0.01	-	0.40 \pm 0.02
SF11 Melted	Fe ^{III} O_h	50.0	0.58 \pm 0.01	1.09 \pm 0.01	-	0.46 \pm 0.03
	Fe ^{III} T_d	50.0	0.32 \pm 0.02	1.21 \pm 0.02	-	0.50 \pm 0.03
SF11 Original	Fe ^{III} T_d	100.0	0.42 \pm 0.01	1.20 \pm 0.01	-	1.03 \pm 0.03

210 hem.: Hematite, mag.: Magnetite, mgh.: Maghemite, T_d : Tetrahedra, O_h : Octahedra, A: Absorption
 211 area,

212 δ : Isomer shift, Δ : Quadrupole splitting, H_{int} : Internal magnetic field, Γ : Line width.

213
 214
 215
 216
 217
 218
 219
 220
 221

222 A. S. Ali *et al*

223